Highly Microporous Carbon from Enteromorpha for High-Performance Aqueous Zinc-chalcogen (S, SeS2) Batteries

Mengmeng Liu+,[a, b] Yan Zhang+,*[a] Zhao Xu,[a] Xuguang Han,[a] Wenshan Gou,[a] Yifei Sun,[a] and Chang Ming Li*[b]

Rechargeable aqueous zinc-chalcogen batteries have become a rising star in the energy storage systems due to the high abundance, low cost and high theoretical specific capacity of the chalcogen cathodes (S, Se). However, there are still some challenges in its practical application, such as low utilization of active substances due to the poor conductivity of chalcogen and sizable volume changes during charging/discharging. In this work, for the first time, nitrogen-doped highly microporous biomass-derived carbon (HMCs-3) was synthesized as a sulfur-loaded cathode for aqueous zinc-chalcogen batteries. A high specific surface area (3349.4 $m^2 g^{-1}$) and a wealthy micropore of

HMCs-3 provide enough space to load the active substances and allow electrolytes to access reaction sites while well alleviating the volume changes of sulfur during the cycling process. As a cathode for aqueous zinc-chalcogen batteries, HMCs-3@S delivers a high reversible discharge capacity (591 $mAh g^{-1}$ at 0.1 $A g^{-1}$), an excellent rate capability (477 $mAh g^{-1}$ at 3 $A g^{-1}$) and good cycling stability (559 $mAh g^{-1}$ after 100 cycles at 1 $A g^{-1}$). The excellent performance of this biomass-derived carbon holds great promise for practical applications in aqueous zinc-chalcogen batteries.

Introduction

Rechargeable aqueous zinc-ion batteries (ZIBs) are promising for energy storage applications due to superior electrochemical performance and extremely high safety advantages. Thus far, conventional aqueous ZIBs with manganese-based,[1] vanadium-based,[1b,2] and Prussian blue analogs[3] as positive electrodes have yielded fruitful research results, but the capacity they can provide is limited. The chalcogens are commercially competitive cathode materials as their high theoretical specific capacity (S: 1675 $mAh g^{-1}$, Se: 675 $mAh g^{-1}$), extensive material source, and low cost.[4] Especially when chalcogens are used as the cathode of the aqueous battery, chalcogen-based battery shows superior kinetics because of the high ionic conductivity of water-based solvents.[5] In recent years, aqueous zinc-chalcogen (Zn-chalcogen) batteries that employed sulfur (S),[6] selenium (Se),[7] and selenium sulfide (Se_xS_y)[8] as the cathodes are anticipated to be the novel generation energy storage devices due to their excellent capacity and conversion mechanism.

A prerequisite for the preparation of chalcogen cathodes is the incorporation of a conductive matrix. Research has shown that the porous carbon hosts can overcome the electrical insulation and buffer the volume expansion amid the cycling for improved battery performance.[9] Therefore, the devise and preparation of superior porous carbon materials as sulfur carriers are significant for the properties of aqueous Zn-chalcogen batteries. Various materials such as fullerene, carbon fiber, nanowires,[10] carbon nanotubes,[11] and graphene[12] have been designed as host frameworks for chalcogenides, but most feedstock comes from non-renewable fossil fuels. It limits the sustainable development of chalcogen-based cathodes to a certain extent and brings environmental and resource problems. In recent years, biomass-derived carbon has stood out among various energy storage electrode materials due to its application advantages such as rich precursor resources, excellent porous structure, and low cost.[13] In addition, natural biomass-derived carbon materials can form in-situ self-doping during the synthesis process, and the doped heteroatoms can increase the active sites of porous material and improving the utilization of active substances.[14] As far as we know, currently, no reports are available on sulfur-loaded biomass-derived porous carbon for composite cathode materials for aqueous Zn-chalcogen batteries.

In this work, we synthesized a porous carbon material with a large surface area (3349.4 $m^2 g^{-1}$) and rich micropores as the chalcogen skeleton using natural biomass Enteromorpha as a precursor, which solved the electrical insulation problem of the chalcogen as well as provided sufficient space for the loading of the chalcogen and buffering the volume expansion in the electrochemical process. The HMCs-3@S cathode delivers a respectable reversible capacity of 591 $mAh g^{-1}$ at 0.1 $A g^{-1}$, offers excellent rate performance of 477 $mAh g^{-1}$ at 3 $A g^{-1}$, as

[a] M. Liu,+ Dr. Y. Zhang,+ Z. Xu, X. Han, W. Gou, Y. Sun
Institute of Advanced Cross-field Science, College of Life Sciences
Qingdao University
266800 Qingdao, (China)
E-mail: yzhang_iacs@qdu.edu.cn
[b] M. Liu,+ Prof. Dr. C. Ming Li
Institute of Materials Science and Devices
School of Materials Science and Engineering
Suzhou University of Science and Technology
215011 Suzhou (China)
E-mail: ecmli@swu.edu.cn
[+] These authors contributed equally to this work.
    Supporting information for this article is available on the WWW under
    https://doi.org/10.1002/batt.202300145

Batteries & Supercaps

Research Article
doi.org/10.1002/batt.202300145

**Chemistry
Europe**

European Chemical
Societies Publishing

well as exhibits stable cycling performance of 559 mAh g^{-1} after 100 cycles (1 A g^{-1}) with average Coulombic efficiency (CE) of 98%. In addition, HMCs-3 also demonstrated good performance (530 mAh g^{-1}) when loaded with SeS$_2$ as the cathode.

Results and Discussion

The microstructures of HMCs-3 and HMCs-3@S were observed using electron microscopy. The morphology of the activated HMCs-3 shows a blocky shape and striated grooves on the carbon surface, as shown in Figure 1(a). TEM images display a multitude of worm-like micropores inside HMCs-3 and a highly amorphous state (Figure 1b and c). The diameter of the synthesized nano-sulfur granule is about 1.5 μm, as shown in Figure S1(a). The diffraction peaks located at 23°, 25.8° and 27.7° in the corresponding XRD patterns can be well pointed to S (PDF#08-0247), proving the successful synthesis of nano-sulfur (Figure S2). The carbon material retained the morphological characteristics of HMCs-3 after loading with nano-sulfur (Figure S1b), and no nano-sulfur particle is detected on its surface, suggesting full encapsulation of sulfur. In addition, the TEM image shows a significant decrease in nanopores (Figure S1c). EDS images (Figure 1d) show that elements C, N, and S elements are uniformly dispersed in the pores of HMCs-3, indicating that the nano-sulfur particles have successfully penetrated the pores of HMCs-3. As a carrier for sulfur-based cathodes, the porous structure of HMCs-3 can provide an efficient channel for ion transport, which is crucial for electrochemical performance.[15]

N$_2$ adsorption-desorption measurements are conducted to measure the specific surface area and pore distribution. HMCs-3 represents a typical type I isotherm, as shown in Figure 2(a). When the value of P/P_0 is less than 0.1, the adsorption volume increases sharply, indicating that HMCs-3 owns a highly microporous structure. The adsorption continues to increase in the relative pressure range of 0.01–0.3, suggesting the existence of small mesoporous structures. The Brunauer-Emmett-Teller (BET) specific surface area of HMCs-3 is 3349.4 m^2 g^{-1}, and the pore volume is 1.73 cm^3 g^{-1}. In Figure S2(a), HMCs-2, and HMCs-4 show similar to type I isothermal curves as HMCs-3 but have lower specific surface areas. The pore size distribution profiles show that the pore size of HMCs-3 is mostly concentrated within 2 nm, with a small amount of distribution in the range of 2–3 nm (Figures 2b and S2b). The above results indicate that HMCs-3 has plenty of micropores and a few small-sized mesopores. In addition, the structural parameters of HMCs-n obtained by activation with different ratios are compared (Table S1). The ultra-high surface area and rich microporous structure of HMCs-3 can provide sufficient space for the loading of sulfur and the adsorption of electrolytes and alleviate the volume expansion of sulfur.[15,16] The specific surface area and pore volume of the carbon material are significantly reduced after sulfur loading (Figure 2a, b), which prove that the nano-sulfur successfully loading into the micropores of the carbon matrix.

The XRD curve of HMCs-3 shows a flat curve with almost no impurity peaks. Two diffraction peaks with weak intensity and broad shape (2θ = 24° and 44°) correspond to the (002) and (100) crystallographic faces of carbon, respectively (Figure 2c). The lower intensity and wider shape of the diffraction peaks reflect that HMCs-3 is a disordered amorphous structure. On the other hand, the graphitization tendency exhibited by HMCs-3 is favorable for conductivity enhancement. No sharp diffraction peaks of S are found in the XRD pattern of HMCs-3@S, which is attributed to full dispersion and confinement in the micropores of the carbon material, resulting in poor crystallinity of sulfur.[17] It agrees well with the results of the EDS image in Figure 1(e). In the Raman spectrum (Figure 2d), two intense peaks at 1337 and 1594 cm^{-1} correspond to the D-band (disordered/defective structure) and the G-band (graphitized structure), respectively. The strength ratio of I_D/I_G
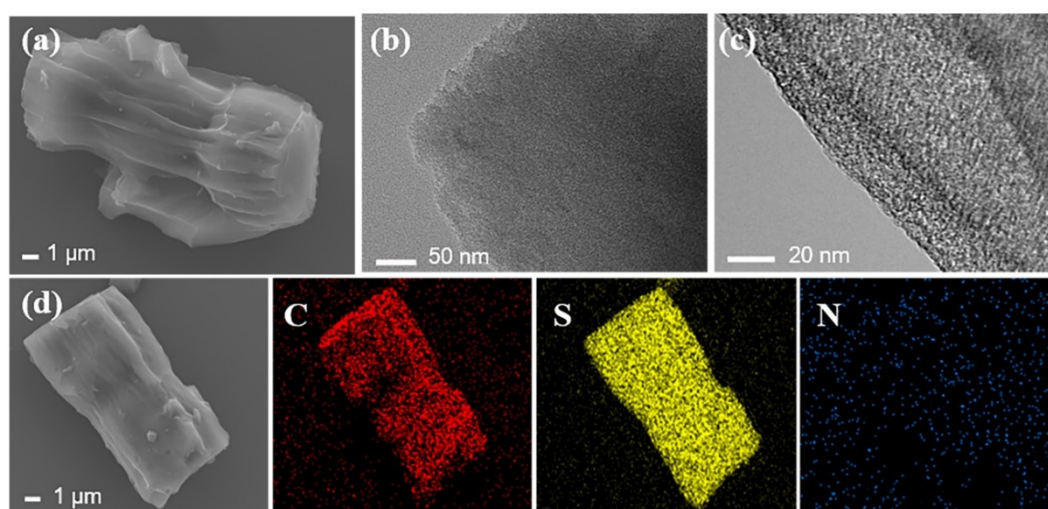

Figure 1. Morphology characterization: a) SEM and b, c) TEM images of HMCs-3; d) EDS images of HMCs-3@S and the corresponding elemental mapping of C, S, and N elements, respectively.
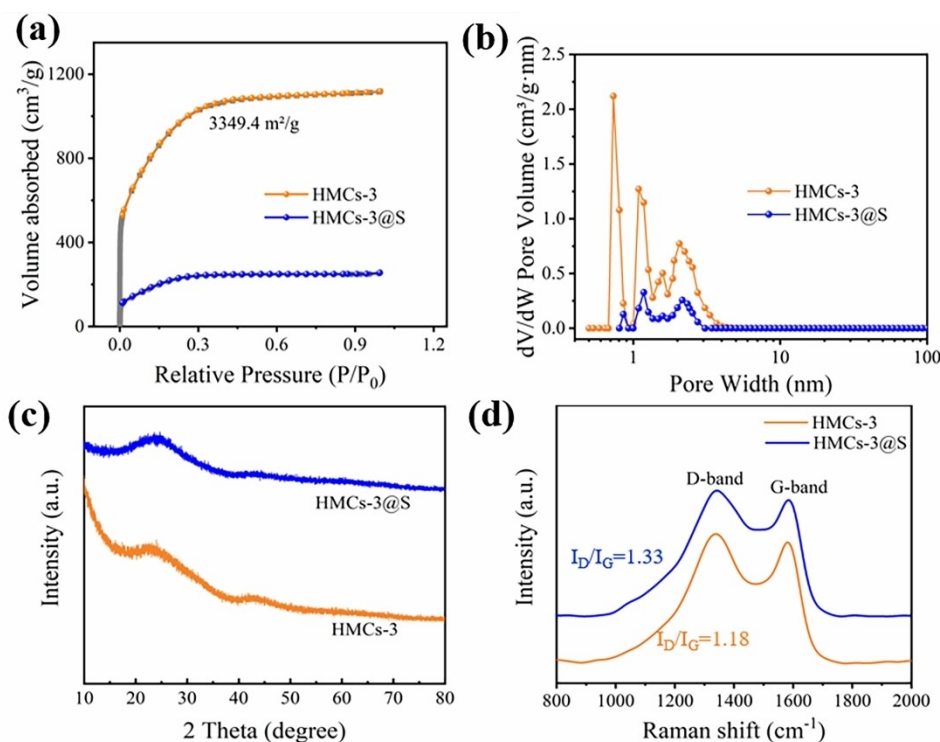
Figure 2. a) N_2 adsorption-desorption isotherms of the HMCs-3 and HMCs-3@S; b) pore size distribution of the HMCs-3 and HMCs-3@S; c) XRD pattern of the HMCs-3 and HMCs-3@S; d) Raman spectra of the HMCs-3 and HMCs-3@S.

can indicate the degree of graphitization of the carbon matrix.[18] The I_D/I_G of HMCs-3 is 1.18, significantly above the currently known commercial active carbon (Norit (AC), $I_D/I_G=$ 0.52). It is further evidence that HMCs-3 exist more defects and is suitable as a host framework for nano-sulfur. After S loading, the higher I_D/I_G of HMCs-3@S is due to the penetration of nano-sulfur into the micropores of HMCs-3, which increases the disorder of carbon. As shown in Figure S3, the sulfur content of the HMCs-3@S was about 48 wt%, as determined by thermogravimetric analysis (TGA).

XPS was performed to evaluate the chemical information on HMCs-3 and HMCs-3@S. As shown in Figure 3(a), HMCs-3 contain mainly C, N, and O elements. There are three peaks in the XPS spectra of C 1s (Figure 3b), which are attributed to C=C/C–C (284.7 eV), C–O/C–N (285.9 eV), and O–C=O (288.3 eV), respectively. The N 1s spectra of HMCs-3 in Figure 3c exhibit two peaks at 400.16 and 401.97 eV, corresponding to pyrrolic N (N-5) at the edge of the graphite plane and graphitic N (N–Q) in the carbon layer, respectively.[13d] The defects caused by the nitrogen atoms may offer more active sites for sulfur, allowing cathode materials to improve both rate performance and capacity.[19] HMCs-3@S exist a characteristic peak of S 2p at 164 eV in addition to C, N, and O (Figure 3a). The S 2p spectrum of HMCs-3@S (Figure 3d) can be fitted with three peaks, including the S $2p_{3/2}$ (164.1 eV), S $2p_{1/2}$ (165.3 eV), and C–SO_x–C (168.78 eV), which confirms that S is successfully loaded into the carbon skeleton.[13d,19]

To investigate the electrochemical properties of HMCs-3@S, we assembled aqueous Zn–S batteries using the prepared

HMCs-3@S composites as a cathode. The GCD curves are shown in Figure 4(a). HMCs-3@S delivers an initial discharge capacity of 592.7 mAh g^{-1} at 0.1 A g^{-1} with a flat discharge plateau of 0.4 V, corresponding to an initial CE of 96%, showing good reversibility. In cyclic voltammetry (CV) curves, the reduction peak at 0.4 V corresponds to the reduction of elemental S to ZnS, and the oxidation peak at 1.45 V is attributed to the oxidation of ZnS to S (Figure 4b). The CV curves of HMCs-3@S remain almost coincident in the subsequent cycles, which demonstrates its excellent reversibility. It also suggests that the rich porous structure of HMCs-3 allows the transport of ions and can alleviate the volume expansion. In addition, HMCs-3@S exhibits a reversible capacity of 568.2 mAh g^{-1} at a current density of 0.1 A g^{-1}. After 50 cycles, a reversible discharge capacity of 559.9 mAh g^{-1} is retained, corresponding to a high-capacity retention of 98.5% (Figure 4c). Figure 4d shows the rate capability of HMCs-3@S at different current densities from 0.1 to 3 A g^{-1}. The reversible discharge capacities of HMCs-3@S at 0.1, 0.5, 1, 2, and 3 A g^{-1} current densities are 721, 535, 505, 487, and 477 mAh g^{-1}, respectively. The capacity retention of HMCs-3@S is 66% when the current density increases from 0.1 to 3 A g^{-1}, which is higher than the other Zn–S batteries mentioned in the Table. S2. As shown in Figure 4(e), the long-term cycling test of HMCs-3@S was conducted at 1 A g^{-1}. The initial reversible capacity of the HMCs-3@S cathode was 455 mAh g^{-1}, yet gradually increased to 591 mAh g^{-1} after 45 cycles, which may be resulted from the gradual wetting of the nano-sulfur by the electrolyte into the microporous network of HMCs-3 during the cycling process. After 100 cycles,
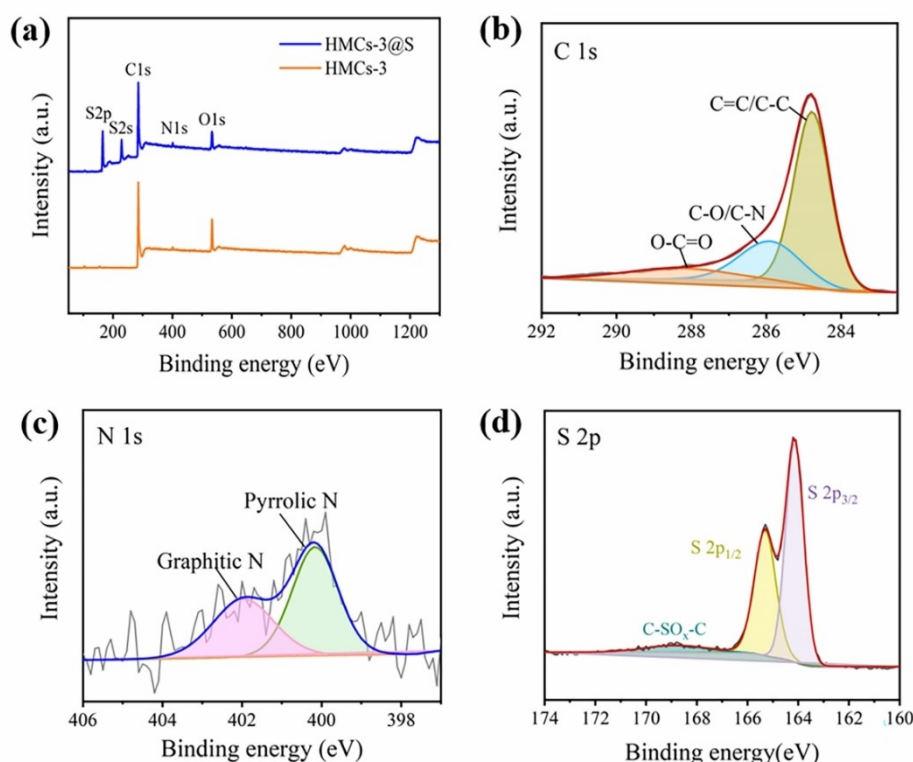
Figure 3. a) XPS survey spectrum of HMCs-3 and HMCs-3@S; b) C 1s high-resolution XPS spectrum of HMCs-3; c) N 1s high-resolution XPS spectrum of HMCs-3; d) S 2p high-resolution XPS spectrum of HMCs-3@S.

HMCs-3@S maintains a specific capacity of 559 mAh g^{-1} with average CE of 98%, which exhibits a reversible conversion between S and ZnS. In addition, a low capacity decay of 0.098% per cycle of HMCs-3@S also highlights the excellent cycle stability compared to the Zn–S batteries reported in Table S2. The excellent cyclic stability and rate capability shown could be ascribed to the unique structure of HMCs-3 (high specific surface area, high porosity) and the stability of its internal structure.

In addition, HMCs-3 was also used as the carbon matrix of SeS$_2$ to evaluate its electrochemical performances. The SeS$_2$ cathode can enhance the reactivity and conductivity of sulfur by utilizing the synergistic interaction between S and Se, thereby improving the electrochemical performance.[8b,20] Similar to HMCs@S, no diffraction peaks of SeS$_2$ were observed in the XRD pattern (Figure S5a). In the XPS spectrum shown in Figure S5b, S and Se elements can be observed, indicating that SeS$_2$ has been loaded into the porous carbon matrix. In addition, the partial overlap between S 2p and Se 3p spectra indicates a strong chemical bonding interaction between S and Se.[8a] The weight ratio of SeS$_2$ was analyzed by the TGA curve in Figure S5d as 53.3 wt%. In addition, the elemental mappings reveal the uniform distribution of SeS$_2$ in HMCs-3 (Figure S6). The electrochemical performance of HMCs-3@SeS$_2$ is shown in Figure 5. HMCs-3@SeS$_2$ demonstrates an initial discharge capacity of 595.9 mAh g^{-1} (1 A g^{-1}), corresponding to an initial CE of 98% and demonstrating excellent cyclic reversibility (Figure 5a). Figure 5(b) presents the CV curves for the first three

cycles, and the overlapping of these curves confirms good reversibility. HMCs-3@SeS$_2$ shows excellent cycle stability with a reversible discharge capacity of 616 mAh g^{-1} and 99% CE even after 50 cycles (Figure 5c). Moreover, HMCs-3@SeS$_2$ demonstrates excellent rate performance, delivering high capacities of 768.3, 714.9, 682.9, 653.5, and 630.2 mAh g^{-1} at current densities of 0.1, 0.5, 1, 2, and 3 A g^{-1}, respectively (Figure 5d). When the current density is reduced to 0.1 A g^{-1}, HMCs-3@SeS$_2$ can recover 91.4% of the discharge capacity. These results indicate that HMCs-3 has good scalability as a carbon matrix for chalcogen cathodes in aqueous Zn-chalcogen battery.

Ex-situ XRD, XPS, and TEM tests are performed to elucidate the reaction mechanism of HMCs-3@S. In Figure 6(a), when HMCs-3@S is discharged to 0.3 V, there is no significant change in diffraction peaks compared with the pristine electrode, suggesting the amorphous structure maintains. Three distinct broad diffraction peaks appear at 28°, 48°, and 56° diffraction angles when HMCs-3@S is discharged to 0.2 V, coinciding with the characteristic peaks of ZnS (JCPDS No. 05-0566). At the fully discharged 0.1 V, the peak signal of ZnS is significantly enhanced, proving the conversion of S to ZnS. During the reverse charging process, the peak intensity of ZnS gradually decreases and completely disappears while charging to 1.6 V, which indicates the reversible conversion between ZnS and S. XPS further demonstrates the conversion mechanism (Figure 6b, c). Two intense Zn peaks at 1020 eV and 1045 eV appear as HMCs-3@S is fully discharged, and they sharply weaken when HMCs-3@S is charged to 1.6 V (Figure 6b). Meanwhile, a
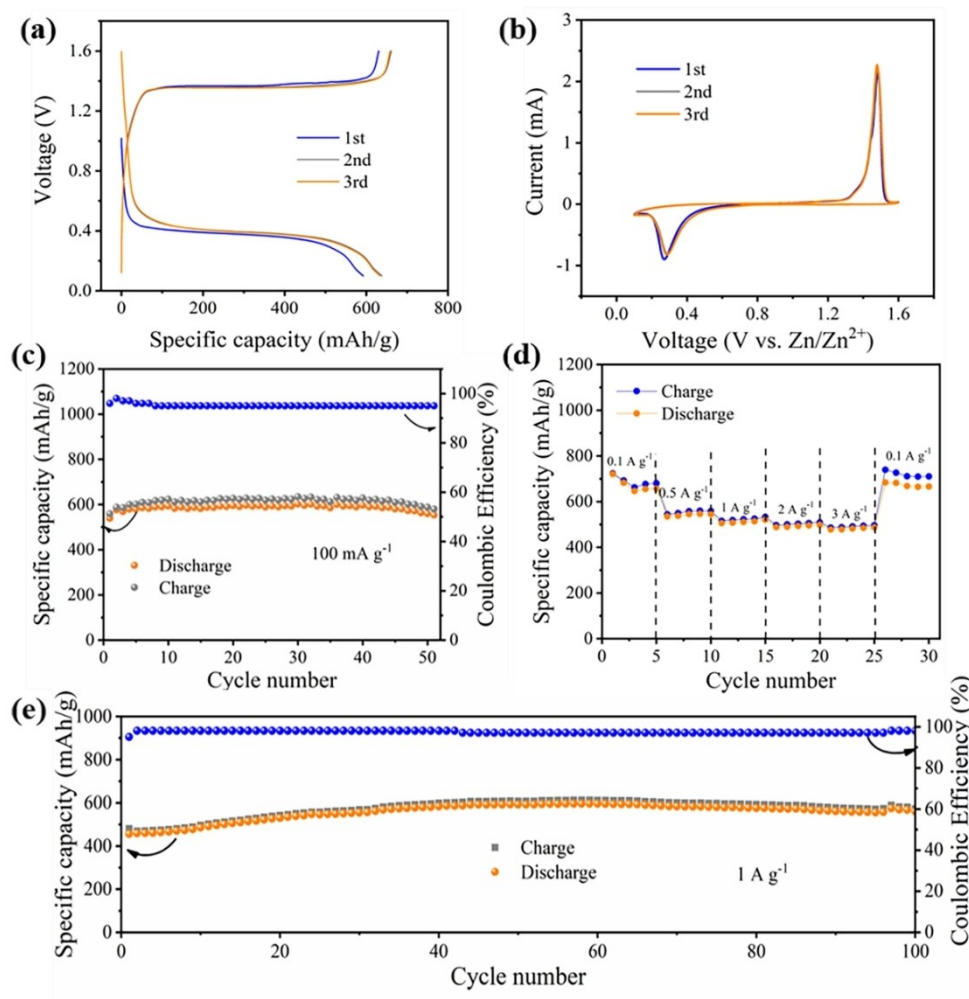
Batteries & Supercaps

Research Article
doi.org/10.1002/batt.202300145

Chemistry
Europe

European Chemical
Societies Publishing

Figure 4. a) Charge and discharge curves of HMCs-3@S cathode; b) CV curves of the HMCs-3@S at 0.05 mV s^{-1}; c) cycling performance of HMCs-3@S at 0.1 A g^{-1}; d) rate performance of HMCs-3@S at various current densities; e) long-term cycling performance of the HMCs-3@S at a current density of 1 A g^{-1}.

distinct S^{2-} signal is detected at 161.5 eV as HMCs-3@S is fully discharged to 0.1 V (Figure 6c). At the fully charged state, the S^{2-} signal diminishes, while a clear characteristic peak of S can be observed. And the low-intensity peaks at 168.8 eV could be ascribed to the S–O bonds of sulfate species arising from the oxidation of active sulfur in air, which leads to slight capacity decay.[6b,21] In addition to XRD and XPS, the conversion reaction was further demonstrated from HRTEM images. Figure 6(d) shows the fully discharged products. The interlayer spacing of 0.314 nm for the discharge product coincides with the (111) lattice plane of ZnS (JCPDS. No. 05-0566), which confirms that the discharge product of the HMCs-3@S electrode is ZnS. The interlayer spacing of 0.322 nm at HMCs-3@S cathode in the fully charged state also fits well with the (040) lattice plane of S (Figure S7).

To explore the mechanism of cycling stability, SEM, TEM, XRD, Raman, and EIS tests were performed on HMCs-3@S electrodes before and after cycling. The surface morphology of HMCs-3@S maintains its original feature after 100 cycles (Figure S8). TEM images (Figure 7a) also confirm that HMCs-3@S does not show structural deformation and pulverization after

cycling. The structure of high-density microporosity is still maintained, which indicates that HMCs-3 possesses good structural stability.[9a] The broad peak corresponding to the (002) lattice plane observed in the XRD spectrum (Figure 7b) illustrates the amorphous nature of the cycled HMCs-3. In addition, as shown in Figure 7(c), no shift occurs in the D-band and G-band of the HMCs-3@S after long cycling. It also suggests that the carbon matrix can keep a stable structure even after long cycles of large currents, further proving its structural stability. In addition, the electrochemical impedance spectra (EIS) are used to further explore the electrochemical behavior of the HMCs-3@S cathode before and after cycling. The R_{ct} at the electrode/electrolyte interface decreased significantly after 100 cycles, as shown in Figure 7(d). This change confirms that the HMCs-3@S composite has excellent conductivity and structural stability, which can ensure quick and stable migration of Zn^{2+} during charging and discharging. Also, this is a crucial reason for the cycling stability of the HMCs-3@S composite electrode.
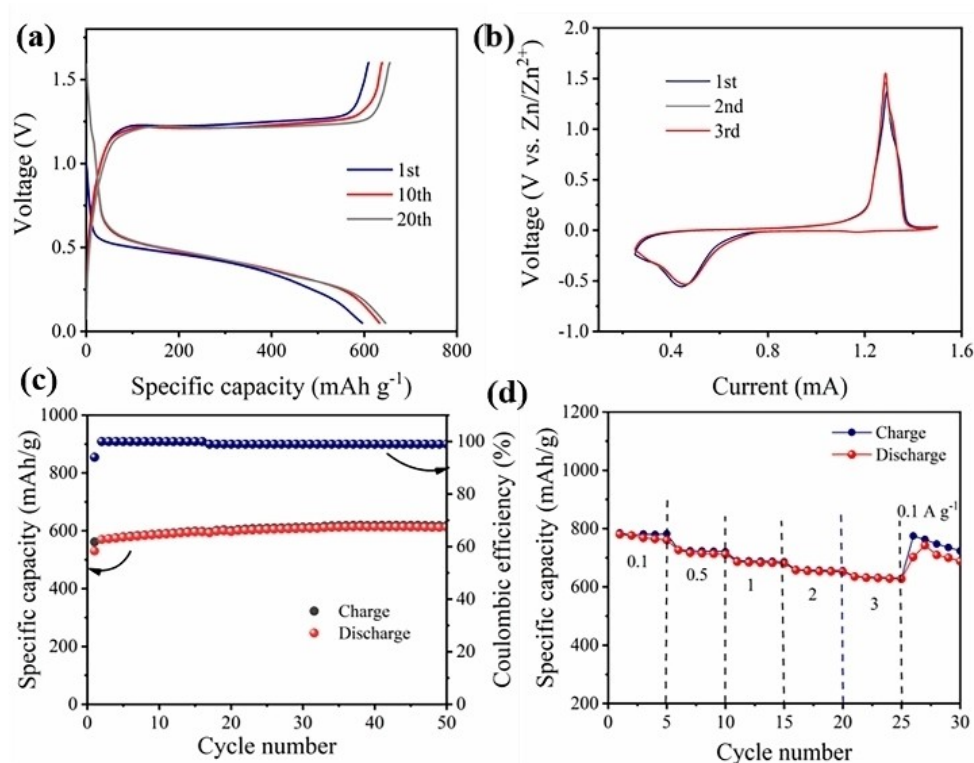
Batteries & Supercaps

Research Article
doi.org/10.1002/batt.202300145

Chemistry Europe
European Chemical
Societies Publishing

Figure 5. (a) Charge and discharge curves of HMCs-3@SeS$_2$ cathode; (b) CV curves of HMCs-3@SeS$_2$ at 0.05 mV s^{-1}; (c) Cycling performance of HMCs-3@SeS$_2$ at 1 A g^{-1}; (d) Rate performance of HMCs-3@SeS$_2$ at various current densities.

Figure 6. a) XRD patterns and of HMCs-3@S at different states; XPS spectra of b) Zn 2p, c) S 2p, and at the pristine, fully discharged and charged state; d) TEM image of HMCs-3@S at fully discharged state.
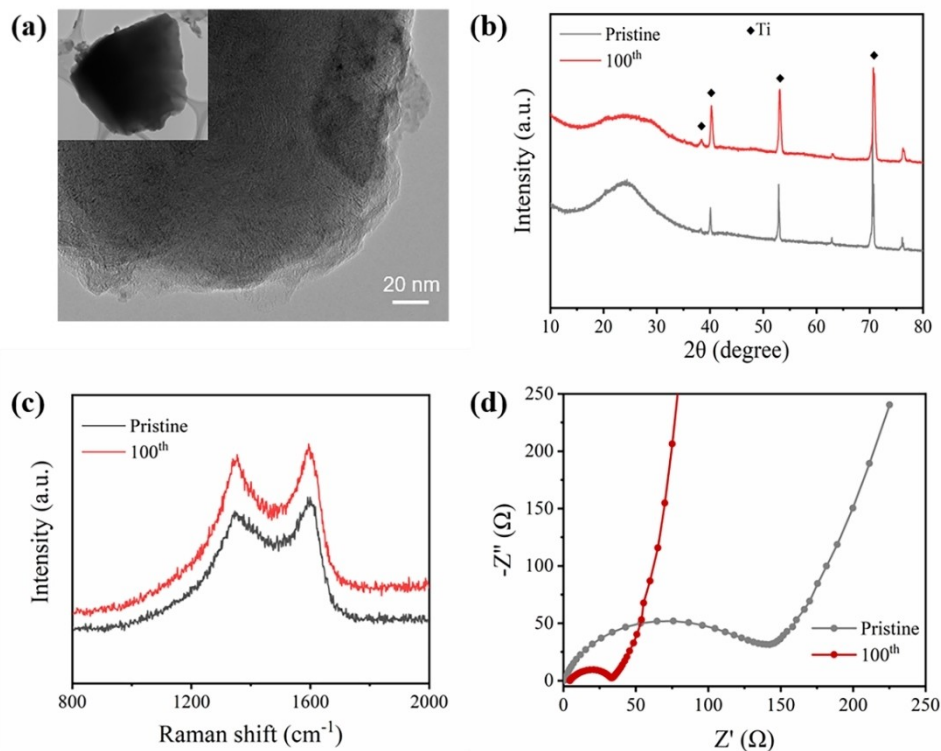
Figure 7. a) TEM images of HMCs-3@S electrode after 100 cycles. b) XRD pattern of HMCs-3@S; c) Raman spectra of HMCs-3@S; d) Nyquist plot of the HMCs-3@S electrode after 100 cycles compared with the fresh electrode.

Conclusions

In summary, this work prepared Enteromorpha-derived porous carbon materials using simple high-temperature carbonization and alkali treatment activation method. It exhibits a high specific surface area, abundant microporous structure, and heteroatomic functional groups. The synergistic effect of these features improves charge storage capacity and ensure efficient transport of ions and electrons. At the same time, it helps to withstand the mechanical stress in electrochemical cycles and effectively alleviates volume expansion. The HMCs-3@S cathode delivered a high reversible capacity (591 mAh g^{-1} at 0.1 A g^{-1}), excellent cycling stability (559 mAh g^{-1} after 100 cycles at 1 A g^{-1}), and superior rate performance. We believe that the excellent electrochemical properties and scalability of low-cost and environmentally friendly biomass-derived carbon provide an opportunity to design high-performance aqueous Zn-chalcogen batteries.

Experimental Section

Materials: The Enteromorpha used in this experiment was collected from the bathing beach in Qingdao, China. The reagents required for the experimental process include potassium hydroxide (KOH, Macklin, China), hydrochloric acid (HCl, Sinopharm Chemical Reagent Co., Ltd., China), polyvinylpyrrolidone ((C_6H_9NO)$_n$, Aladdin, China), absolute ethanol (C_2H_6O, Macklin, China), sodium thiosulfate ($Na_2S_2O_8$, Aladdin, China), and zinc trifluoromethanesulfonate (Zn-(OTF)$_2$, Aladdin, China). All the above reagents are analytically pure (AR) and can be used directly. The inert gases are 99.99% pure N_2 and Argon.

Preparation of the HMCs-n: First, the collected Enteromorpha was washed with deionized water (DI water) to remove impurities, then freeze-dried and chopped. The treated Enteromorpha was put into an alumina crucible and heated to 500 °C under N_2 atmosphere in a tubular resistance furnace for 1 h (5 °C min^{-1}). Then, KOH was used to activate the calcined precursor. The KOH was thoroughly mixed with carbon powder (mass ratio n:1). Calcined the blended carbon/activator at 800 °C for 1 h under an atmosphere of N_2 atmosphere, and the temperature increase rate was 3 °C min^{-1}. Whereafter, the activated samples were etched using dilute hydrochloric acid solution, then rinsed with a large amount of DI water to pH neutrality at 60 °C, and dehydrated overnight at 80 °C. The final carbon materials were named HMCs-n, n denoting the proportion of KOH to carbon powder.

Preparation of the HMCs@S composite: In a typical process, 2.335 g of $Na_2SO_3 \cdot 5H_2O$ was weighed and dissolved completely into 150 mL of DI water, then 3.3 g of PVP was added to the solution and stirred until it was completely dissolved. Whereafter, 1.2 mL concentrated HCl was addition gradually, stirred for 2 h, rinsed repeatedly with DI water, then dried overnight at 80 °C to obtain nano-sulfur powder. The prepared HMCs-n and nano-sulfur powder (mass ratio 1:1) were mixed well in an agate mortar. The carbon-sulfur mixed powder was heat-treated overnight at 155 °C under Ar at a 3 °C min^{-1} ramp rate to disperse the nano-sulfur into pores of carbon material. The HMCs-n@S cathode material was obtained.

Batteries & Supercaps

Research Article
doi.org/10.1002/batt.202300145

Chemistry Europe
European Chemical
Societies Publishing

Supporting Information

Supporting Information is available from the Wiley Online Library or from the author.

Conflict of Interests

The authors declare no conflict of interest.

Data Availability Statement

The data that support the findings of this study are available from the corresponding author upon reasonable request.

[1] a) H. Pan, Y. Shao, P. Yan, Y. Cheng, K. S. Han, Z. Nie, C. Wang, J. Yang, X. Li, P. Bhattacharya, K. T. Mueller, J. Liu, *Nat. Energy* **2016**, *1*, 16039; b) P. Hu, T. Zhu, X. Wang, X. Wei, M. Yan, J. Li, W. Luo, W. Yang, W. Zhang, L. Zhou, Z. Zhou, L. Mai, *Nano Lett.* **2018**, *18*, 1758–1763.

[2] J. H. Jo, Y.-K. Sun, S.-T. Myung, *J. Mater. Chem. A* **2017**, *5*, 8367–8375.

[3] G. Zampardi, F. La Mantia, *Curr. Opin. Electrochem.* **2020**, *21*, 84–92.

[4] Y. Wang, X. Li, W. Wang, H. Yan, S. Xin, Y. Guo, *Sci. China Chem.* **2020**, *63*, 1402–1415.

[5] a) J. Liu, W. Zhou, R. Zhao, Z. Yang, W. Li, D. Chao, S. Z. Qiao, D. Zhao, *J. Am. Chem. Soc.* **2021**, *143*, 15475–15489; b) L. Zhang, Y. Liu, *Batteries* **2023**, *9*, 62; c) Y. Guo, R. Chua, Y. Chen, Y. Cai, E. J. J. Tang, J. J. N. Lim, T. H. Tran, V. Verma, M. W. Wong, M. Srinivasan, *Small* **2023**, e2207133.

[6] a) Y. Zhao, D. Wang, X. Li, Q. Yang, Y. Guo, F. Mo, Q. Li, C. Peng, H. Li, C. Zhi, *Adv. Mater.* **2020**, *32*, e2003070; b) W. Li, K. Wang, K. Jiang, *Adv. Sci.* **2020**, *7*, 2000761; c) C. Dai, X. Jin, H. Ma, L. Hu, G. Sun, H. Chen, Q. Yang, M. Xu, Q. Liu, Y. Xiao, X. Zhang, H. Yang, Q. Guo, Z. Zhang, L. Qu, *Adv. Energy Mater.* **2021**, *11*, 2003982; d) H. Zhang, Z. Shang, G. Luo, S. Jiao, R. Cao, Q. Chen, K. Lu, *ACS Nano* **2022**, *16*, 7344–7351; e) D. Liu, B. He, Y. Zhong, J. Chen, L. Yuan, Z. Li, Y. Huang, *Nano Energy* **2022**, *101*, 107474; f) Z. Xu, Y. Zhang, W. Gou, M. Liu, Y. Sun, X. Han, W. Sun, C. Li, *Chem. Commun.* **2022**, *58*, 8145–8148; g) A. Amiri, R. Sellers, M. Naraghi, A. A. Polycarpou, *ACS Nano* **2023**, *17*, 1217–1228; h) T. Zhou, H. Wan, M. Liu, Q. Wu, Z. Fan, Y. Zhu, *Mater. Today Energy* **2022**, *27*, 101025; i) M. Yang, Z. Yan, J. Xiao, W. Xin, L. Zhang, H. Peng, Y. Geng, J. Li, Y. Wang, L. Liu, Z. Zhu, *Angew. Chem. Int. Ed.* **2022**, *61*, e202212666; j) W. Zhang, M. Wang, J. Ma, H. Zhang, L. Fu, B. Song, S. Lu, K. Lu, *Adv. Funct. Mater.* **2023**, *33*, 2210899; k) G. Chang, J. Liu, Y. Hao, C. Huang, Y. Yang, Y. Qian, X. Chen, Q. Tang, A. Hu, *Chem. Eng. J.* **2023**, *457*, 141083.

[7] Z. Chen, F. Mo, T. Wang, Q. Yang, Z. Huang, D. Wang, G. Liang, A. Chen, Q. Li, Y. Guo, X. Li, J. Fan, C. Zhi, *Energy Environ. Sci.* **2021**, *14*, 2441–2450.

[8] a) W. Li, X. Jing, Y. Ma, M. Chen, M. Li, K. Jiang, D. Wang, *Chem. Eng. J.* **2021**, *420*, 129920; b) W. Li, Y. Ma, P. Li, X. Jing, K. Jiang, D. Wang, *Adv. Funct. Mater.* **2021**, *31*, 2101237.

[9] a) X. L. Huang, S. X. Dou, Z. M. Wang, *Energy Storage Mater.* **2022**, *45*, 265–280; b) M. Zhao, B. Q. Li, X. Q. Zhang, J. Q. Huang, Q. Zhang, *ACS Cent. Sci.* **2020**, *6*, 1095–1104; c) S. Feng, Z. H. Fu, X. Chen, Q. Zhang, *InfoMat* **2022**, *4*, e12304.

[10] Z. Li, Q. He, X. Xu, Y. Zhao, X. Liu, C. Zhou, D. Ai, L. Xia, L. Mai, *Adv. Mater.* **2018**, *30*, e1804089.

[11] a) Y. Zhao, W. Wu, J. Li, Z. Xu, L. Guan, *Adv. Mater.* **2014**, *26*, 5113–5118; b) L. Sun, D. Wang, Y. Luo, K. Wang, W. Kong, Y. Wu, L. Zhang, K. Jiang, Q. Li, Y. Zhang, J. Wang, S. Fan, *ACS Nano* **2016**, *10*, 1300–1308.

[12] a) T. Wang, Q. Zhang, J. Zhong, M. Chen, H. Deng, J. Cao, L. Wang, L. Peng, J. Zhu, B. Lu, *Adv. Energy Mater.* **2021**, *11*, 2100448; b) Y. Zhang, P. Zhang, S. Zhang, Z. Wang, N. Li, S. R. P. Silva, G. Shao, *InfoMat* **2021**, *3*, 790–803.

[13] a) P. Liu, Y. Wang, J. Liu, *J. Energy Chem.* **2019**, *34*, 171–185; b) G. Yuan, W. Zhang, H. Li, Y. Xie, H. Hu, Y. Xiao, Y. Liang, Y. Liu, W. R. Liu, M. Zheng, *J. Colloid Interface Sci.* **2020**, *580*, 638–644; c) P. Xia, W. Lei, X. Wang, Z. Luo, Y. Pan, Z. Ma, *J. Alloys Compd.* **2020**, *832*, 153692; d) Q. Xiao, G. Li, M. Li, R. Liu, H. Li, P. Ren, Y. Dong, M. Feng, Z. Chen, *J. Energy Chem.* **2020**, *44*, 61–67; e) Q. Gao, D. Li, X. Liu, Y. Wang, W. Liu, M. Ren, F. Kong, S. Wang, R. Zhou, *Electrochim. Acta* **2020**, *335*, 135642.

[14] A. Gopalakrishnan, S. Badhulika, *J. Power Sources* **2020**, *480*, 228830.

[15] Z. Bi, Q. Kong, Y. Cao, G. Sun, F. Su, X. Wei, X. Li, A. Ahmad, L. Xie, C.-M. Chen, *J. Mater. Chem. A* **2019**, *7*, 16028–16045.

[16] H. Yuan, T. Liu, Y. Liu, J. Nai, Y. Wang, W. Zhang, X. Tao, *Chem. Sci.* **2019**, *10*, 7484–7495.

[17] J. S. Yeon, S. H. Park, J. Suk, H. Lee, H. S. Park, *Chem. Eng. J.* **2020**, *382*, 122946.

[18] H. Wan, X. Ju, T. He, T. Chen, Y. Zhou, C. Zhang, J. Wang, Y. Xu, B. Yao, W. Zhuang, X. Du, *J. Alloys Compd.* **2021**, *863*, 158078.

[19] J. Li, J. Zhou, T. Wang, X. Chen, Y. Zhang, Q. Wan, J. Zhu, *Nanoscale* **2020**, *12*, 8991–8996.

[20] J. Zhang, Z. Li, X. W. D. Lou, *Angew. Chem. Int. Ed.* **2017**, *56*, 14107–14112.

[21] M. Cui, J. Fei, F. Mo, H. Lei, Y. Huang, *ACS Appl. Mater. Interfaces* **2021**, *13*, 54981–54989.